A miniature triaxial apparatus for investigating the micromechanics of granular soils with in-situ X-ray micro-tomography scanning

Z. Cheng[1], J.F. Wang[2, 3], M.R. Coop[4] and G.L. Ye[5]

[1] Ph.D., Research Associate
Department of Architecture and Civil Engineering,
City University of Hong Kong, Tat Chee Avenue, Kowloon, Hong Kong

[2]Associate Professor (Corresponding Author)
Department of Architecture and Civil Engineering,
City University of Hong Kong, Hong Kong
Tel: (852) 34426787, Fax (852) 34420427
E-mail: jefwang@cityu.edu.hk
Address: B6409, Academic 1, City university of Hong Kong,
Tat Chee Avenue, Kowloon, Hong Kong
[3]Shenzhen Research Institute of City University of Hong Kong, Shenzhen, China

[4]Professor
Department of Civil, Environmental and Geomatic Engineering,
University College London, Gower Street, London, UK

[5]Professor
Department of Civil Engineering,
Shanghai Jiaotong University,
Dongchuan Road, Minhang District, Shanghai, China

Abstract: The development of a miniature triaxial apparatus is presented. In conjunction with an X-ray micro-tomography (termed as X-ray μCT hereafter) facility and advanced image processing techniques, this apparatus can be used for in-situ investigation of the micro-scale mechanical behavior of granular soils under shear. The apparatus allows for triaxial testing of a miniature dry sample with a size of $8 \times 16\ mm$ (diameter × height). In-situ triaxial testing of a 0.4~0.8 mm Leighton Buzzard sand (LBS) under a constant confining pressure of 500 kPa is presented. The evolutions of local porosities (i.e., the porosities of regions associated with individual particles), particle kinematics (i.e., particle translation and particle rotation) of the sample during the shear are quantitatively studied using image processing and analysis techniques. Meanwhile, a novel method is presented to quantify the volumetric strain distribution of the sample based on the results of local porosities and particle tracking. It is found that the sample, with nearly homogenous initial local porosities, starts to exhibit obvious inhomogeneity of local porosities and localization of particle kinematics and volumetric strain around the peak of deviatoric stress. In the post-peak shear stage, large local porosities and volumetric dilation mainly occur in a localized band. The developed triaxial apparatus, in its combined use of X-ray μCT imaging techniques, is a powerful tool to investigate the micro-scale mechanical behavior of granular soils.

Key words: Triaxial apparatus; X-ray μCT; in-situ test; micro-scale mechanical behavior; granular soils

1 Introduction

Micro-scale mechanical behavior (e.g., particle crushing and particle rearrangement) plays a very important role in the macro-scale mechanical behavior of granular soils. Evidence has shown that by changing particle size distribution and pore structures, particle crushing and particle rearrangement lead to significant settlement and change of hydraulic conductivity in engineering where stress levels are high; for example, driven piles and high rock-fill dams [1-3]. It has been found that shear-induced dilation and strain softening tend to occur in dense sands under low confining pressures, because of particle rearrangement in the shear band. Meanwhile, shear-induced compression and strain hardening are likely to appear in loose sands under high confining pressures due to particle crushing [4, 5]. The critical state of a loaded sand in which particle crushing takes place can also be interpreted as an equilibrium state between the dilation caused by particle rearrangement and the compression caused by particle crushing [6]. Therefore, investigation into the micro-scale mechanical behavior is of great importance for achieving a full understanding of the macro-scale mechanical behavior, and for developing advanced constitutive models incorporating the corresponding micromechanical mechanisms.

Conventional and advanced triaxial apparatuses have been widely used to evaluate the shear strength and stiffness of granular soils. However, because of the inability to distinguish and characterize individual grains inside a sample in triaxial testing, they cannot be used independently to study the micro-scale mechanical behavior (e.g., grain rearrangement and grain morphology change) of granular soils. Recently, advanced apparatuses have been developed to measure the grain-scale friction coefficients and stiffness, which provides important experimental support for the discrete element modeling (DEM) of micro-scale mechanical behavior of granular materials [7, 8]. DEM was first introduced into the geotechnical field by

Cundall and Strack [9], who modeled each soil particle with a single circle (or sphere). Their model could reproduce the overall macro-scale mechanical behavior of granular soils but led to over-rotation of particles, because the simplified model did not take into consideration the effects of particle shape. Although the efforts made during the last two decades have helped to achieve more realistic particle rotation in DEM modeling [10-17], the modeling of real particle rotation requires the incorporation of real particle shapes and the development of sophisticated contact models, which makes the calculation highly intensive.

The development of optical equipment and imaging techniques (e.g., the microscope, laser-aided tomography, X-ray computed tomography (termed as X-ray CT hereafter) and X-ray μCT) has provided many opportunities for experimental examination of the micro-scale mechanical behavior of granular soils. Via acquisition and analysis of images of soil samples in triaxial testing, these equipment and techniques have been increasingly used in the investigation of soil microstructures [18-24]. These studies have enhanced the understanding of the micro-scale mechanical behavior of granular soils. However, in most of these studies, images were acquired before and after testing, which only allows for the interpretation of the micro-scale mechanical behavior in two loading states (i.e., prior to and after tests). To capture the full micro-scale mechanical behavior of granular soils, image acquisition should be carried out throughout the tests, which requires the development of an apparatus for in-situ testing. Here, in-situ testing refers to CT scanning and image acquisition at the same time of triaxial testing. In recent years, only a very limited number of triaxial devices have been designed for use in conjunction with X-ray CT (or μCT) to conduct in-situ triaxial tests [25-32]. These devices have been used for investigating the micro-scale characteristics changes within granular materials throughout tests (e.g., void ratios, strain distribution, particle kinematics and inter-particle contacts). Specifically,

in its combined use of advanced image processing and analysis techniques such as digital image correlation (DIC) techniques, in-situ testing allows the experimental measurement of strain distribution of soils [32, 33]. Thus, the in-situ testing triaxial apparatus has become a powerful tool to unravel the micro-mechanism of failure of soils subjected to loading.

This paper presents the development of a novel miniature apparatus for in-situ triaxial testing. The detailed design of this apparatus is presented to facilitate the building of such an apparatus to conduct micromechanical experiments on soils. A main advantage of this apparatus, over many of the currently existing apparatuses for in-situ triaxial testing, is its high confining pressure capacity (i.e., up to 2,000 kPa). Meanwhile, a novel method is presented to quantify the strain localization of granular soils. In the following context, we first introduce the principle of X-ray CT (or μCT) and the main considerations for applying it to in-situ triaxial testing. Subsequently, the detailed design of this apparatus is described. Finally, a demonstration triaxial test is carried out on a uniformly graded sample of Leighton Buzzard sand (LBS). The evolutions of local porosities, particle kinematics and volumetric strain distribution of the sample throughout the test are quantitatively studied, and the results are then presented.

2 X-ray CT (μCT) and in-situ triaxial test apparatus

X-ray CT (or μCT) has been widely used to scan 3D CT images of objects. An X-ray CT (or μCT) facility is generally composed of an X-ray source, a rotation stage and a detector. Fig. 1 shows a schematic of a typical parallel beam X-ray μCT facility used for imaging a sample. During operation of the setup, the sample is rotated by the rotation stage across 180° (or 360°) to acquire a series of 2D projections at different angles. These 2D projections are then used to reconstruct a 3D CT image of the sample.

The 3D CT image is determined according to the attenuation coefficient distribution of the sample, based on Beer's law. According to Beer's law, for monochromatic X-rays passing through an object, there is an exponential relationship between the ratio of the emitted X-ray intensity I_0 to the detected X-ray intensity I, and the multiplication of attenuation coefficients u_i with thickness d_i, given by:

$$\frac{I_0}{I} = exp(\sum u_i d_i), \quad (1)$$

where d_i is the material thickness (i.e., the thickness of material i within which the attenuation coefficient u_i is constant) of the object along the path of the X-rays.

A series of such equations can be obtained according to the 2D projections at different angles. A solution to these equations gives the attenuation coefficient distribution, used to determine the intensity values of a CT image of the sample. Different materials generally have different intensity values in a CT image due to their respective attenuation coefficients, which are closely related to their densities. For example, with respect to intensity values soil particles are higher than water, and water is higher than air.

To make use of these properties in in-situ triaxial testing, apparatuses are generally fixed on the rotation stage when they supply loads to samples. A triaxial apparatus for use with an X-ray CT (or μCT) facility generally differs from the conventional triaxial apparatus as follows. Firstly, the apparatus should be very light so that it falls within the loading capacity of the rotation stage of the X-ray CT (or μCT) facility. Secondly, the X-ray CT (or μCT) facility does not allow the triaxial apparatus to have any tie bars around the confining chamber, as these tie bars would obstruct the X-ray beam. Finally, the sample should be small enough to ensure that it remains within the scanning area during the rotation.

Because of the particular requirements (e.g., weight limitations due to the loading capacity of the rotation stages, and geometric restrictions) of the X-ray CT (or μCT) facilities, a light and highly transparent acrylic, Plexiglas or polycarbonate cell is usually used to provide a confining pressure to a sample. For example, Otani and colleagues [29] adopted an acrylic cylindrical cell in their triaxial apparatus which has a spatial resolution of 200 μm and a confining stress capacity of 400 kPa for samples with a size of 50×100 mm (diameter × height). To acquire a higher spatial resolution and a full-field scanning of samples, some authors [26, 31] used a smaller-sized cell (high-spatial resolution X-ray μCT scanners generally have a very small scanning area), in which a much higher confining pressure capacity is also achieved. These features allow the in-situ triaxial testing of granular soils under high confining pressure, and imaging and characterization of their breakage behavior with high spatial resolution. For this purpose, a similar small-sized triaxial cell is adopted in the apparatus presented in the following sections.

3 Triaxial apparatus design

3.1 Schematic of triaxial apparatus

A miniature triaxial system is specially fabricated to incorporate the features stated in Section 2 for use with the X-ray μCT scanner at SSRF. Figs. 2(a) and 2(b) schematically show the triaxial system and a photograph of the apparatus, respectively. As shown in Fig. 2(a), similar to the conventional triaxial system, this triaxial system comprises an axial loading device (i.e., the stepping motor and the screw jack), a confining pressure offering device (i.e., the chamber and the GDS pressure controller) and a data acquisition and controlling system. Note that the triaxial system is used for testing dry samples, and the back pressure valve is used to create suction

inside samples in the sample preparation process. In the current paper, triaxial test of dry samples is used to explore the soil mechanical behavior under drained shear conditions. Meanwhile, the measurement of sample volume change with high-resolution X-ray μCT also allows the absence of water within the sample. Furthermore, the absence of water will also reduce the technical difficulty of image processing and analysis. For these reasons, dry samples are used. The apparatus shown in Fig. 2(b) is about 520 mm in height and 20 kg in weight. The sample size required for the apparatus is 8×16 mm (diameter $\times$ height), and is dictated by consideration of the use of high spatial resolution and the representativeness of a sample, which requires an adequate number of grains inside. While the X-ray μCT scanner at SSRF can offer a high spatial resolution of up to several microns (e.g., 6.5 μm), it has a rather small scanning area (e.g., 11 mm in width and 4.888 mm in height). However, the representativeness of a sample requires that the sample-to-size ratio (i.e., the ratio of specimen diameter to maximum particle size) is larger than six [34, 35]. Note that the use of small sample size may influence the macro-scale mechanical response of the material [36, 37]. It was shown in a comprehensive DEM study by Wang and Gutierrez [36] that as long as a uniform shear banding across the entire sample dimension (i.e., no progressive shear failure) occurs, the sample size can be regarded to be acceptable and the boundary-measured stress-strain curve is representative of the true shear strength of the granular material and does not contain artificial lateral boundary effects. There is no clear evidence of progressive failure within the sample in this study, as will be shown in Section 4. Therefore, its boundary effects are not considered to be significant. In fact, such a practice has also been adopted in many other studies for investigating grain-scale kinematics, inter-particle contacts, and fabrics, etc. [38-41]. A more detailed description of the triaxial system is presented in the following sections.

3.2 Axial loading device

The axial loading device is composed of a rotational stepping motor and a made-to-order screw jack driven by a worm and a worm gear. Fig. 3 shows a closer view of the axial loading device. The rotational stepping motor can offer a maximum torque of 117.9 $N \cdot cm$ and a rotation speed ranging from 0.1318 to 5,110 deg/s. In combination with a screw jack having a speed reduction ratio of 16:1, and a worm drive with a speed reduction ratio of 10:1, the stepping motor can provide a maximum axial force of up to 5 kN and an axial loading speed ranging from 1 to 1,000 $\mu m/min$. Note that in order to resist the reaction forces acting on the worm shaft from the worm along the axial and the radial directions, a pair of axial thrust bearings and radial thrust bearings, respectively, are used.

Below the screw jack, a piston shaft is connected to the screw jack via a load cell and two screw adaptors (see Fig. 2(b)). It should be noted that the axial force measured by the load cell incorporates the friction of the piston shaft, and this is assumed to be constant during the movement of piston shaft. A round-ended loading ram (i.e., the piston shaft) contacting a flat top platen (i.e., the cushion plate shown in Fig. 2(a)) is adopted to transfer the motion from the stepping motor to a sample.

3.3 Confining pressure offering device

The confining pressure is transmitted through water and is offered by a GDS pressure controller (see Fig. 2(a)) with a confining pressure of up to 2,000 kPa. In order to supply the sample with a constant pressure, the apparatus requires a good seal performance. Fig. 4 shows a schematic of the seal design of the chamber. The chamber is fabricated with polycarbonate and has an I-shaped section and a thickness of 20 mm. Different sealing types are incorporated to prevent

leakage with the use of O-rings. On the interfaces between the chamber and the plates (i.e., the base plate and the chamber top plate), and the interface between the piston shaft and the piston shaft sleeve, radial seals are used. An axial seal is utilized between the chamber top plate and the piston shaft sleeve. Additionally, two sealing gaskets are installed on the chamber to prevent leakage from the two cell pressure valve holes, through which the cell pressure fluid is injected.

It is worth noting that the apparatus has no tie bars around the chamber (See Fig. 2(b)). In addition to constant water pressure, the chamber is also subjected to a tensile force along its axis when a deviatoric stress is applied on the sample. This may result in an axially tensile deformation of the chamber. Given that the tensile elastic modulus E_s of the polycarbonate is 2,300 MPa, the axially tensile deformation of the chamber can be estimated by:

$$\omega_c = \frac{A_s q}{A_c E_s} L_c \delta_A, \tag{2}$$

where A_c (A_c= 2,513.3 mm^2) and A_s (A_s= 54.7 mm^2) are the section area of the chamber and the designed sample, respectively. L_c (L_c = 50 mm) is the length of the chamber, while q and δ_A are the deviatoric stress and the sample area expansion factor (i.e., the ratio of the average section area of the deformed sample to A_s), respectively.

This deformation is rather small ($\omega_c \leq 5.68\ \mu m$) if the deviatoric stress is lower than 10 MPa. This is negligible when compared to the axial deformation of the sample ω_s= 80 μm (suppose that the deviatoric stress reaches its peak at the axial strain of 0.5% and δ_A= 1.2).

3.4 Data acquisition and controlling system

Fig. 5 shows a photograph of the data acquisition and controlling system, which comprises a data logger, a micro-computer, a miniature load cell with a capacity of up to 10 kN, and a LVDT with

227 a measurement range of 10 mm. The load cell and the LVDT are connected to the data logger
228 through the port shown in Fig. 5. A specially written code is used to send commands from the
229 computer to the data logger to record the axial force and deformation, and to control the axial
230 loading. Similar data controlling systems have also been used in single particle compression tests
231 [42, 43].

232 **3.5 Sample maker**

233 A sample maker is designed to form samples with a size of $8 \times 16\ mm$ (diameter × height), as
234 shown in Fig. 6. The sample maker is constructed from two pieces of stainless steel molds with a
235 semi-cylindrical inner surface, locked by four screws. The two mold parts have the same size,
236 except for a nozzle connected to one half to increase suction inside. The large flat contact surface
237 is polished to improve the seal performance. The conventional air pluviation method is used to
238 prepare the sample as shown in Fig. 7. This process includes the position of a porous stone and a
239 membrane (Fig. 7A), the installation of the sample maker and the fixing of the membrane (Figs.
240 7B and 7C), the filling of sand grains and the installation of a cushion plate (Figs. 7D and 7E),
241 and finally the removal of the sample maker (Fig. 7F).

242 **4 Triaxial test on LBS sand**

243 **4.1 Test material and synchrotron radiation facility setup**

244 An in-situ triaxial compression test is conducted using the developed triaxial apparatus in
245 combination with the synchrotron X-ray μCT scanner at SSRF. The testing material is a
246 uniformly graded LBS with a particle diameter of 0.4~0.8 mm. The LBS sample has an initial
247 porosity of 0.343 (i.e., a relative density of 127.7%), which is measured from the CT image of
248 the sample after the isotropic consolidation under a confining stress of 500 kPa. Figs. 8(a) and

8(b) show a photograph of the triaxial apparatus being used in conjunction with the synchrotron radiation facility, and a schematic of the connection between them, respectively. The X-ray source has an energy of 25 Kev, and the detector has a spatial resolution of 6.5 μm. This permits a high contrast between sand grains and air voids in the CT images of the sample. In each scan, four sections are required for the full-field imaging of the 16 mm-high sample, because the scanning window of the detector is 4.888 mm in height, and an overlap between any two consecutive sections is required to stitch them together. This is achieved by adjusting the height of the apparatus for different sections using a motor-controlled lifting device, which is fixed upon the board with an alumina plate and has a load capacity of 50 kg, as seen in Fig. 8(b). Above the lifting device, a tilting table positions the sample rotation plane parallel to the X-ray beam. The rotation stage is placed above the tilting table. It has a load capacity of 60 kg and enables the entire apparatus to be rotated with a constant speed of up to $10°/s$.

During the test, the LBS sample is first compressed isotropically to a stress of 500 kPa by the GDS pressure controller, and then loaded axially at a constant rate of 33.34 um/min by the motor. Except for the state prior to shear (i.e., the isotropic compression state), the loading is paused (i.e., the axial displacement is stopped) at different loading states (i.e., axial strains of 0.98%, 4.94%, 10.40%, 15.34%) for CT scan. In each loading state, as the rotation stage rotates the whole apparatus at a constant rate across 180°, the X-ray beam and the detector work to record the CT projections of the sample at different angles. About 1,080 projections are recorded for each section. Due to the powerful X-ray source and the use of an exposure time of 0.08s, a full-field scan of the sample at each loading state takes about 15 min.

4.2 Test results

271 Figs. 9(a) and 9(b) show the stress–strain curves of the tested LBS sample, where the scanning
272 points are marked with circles. As seen in Fig. 9(a), the deviatoric stress (i.e., $\sigma_1 - \sigma_3$) reaches
273 its peak at around the third scan (i.e., at the axial strain of 4.94%). Note that there is a significant
274 drop of the deviatoric stress during each scan. This is due to stress relaxation caused by the pause
275 of loading during a scan. The deviatoric stress increases rapidly to the value before the drop,
276 when the sample is reloaded after the scan. Overall, the sample exhibits a dilation behavior
277 during the shear after a compression in the pre-peak shear increment of 0~0.98%, as shown in
278 Fig. 9(b). Note that the GDS equipment is not used to measure the sample volumetric strain
279 because of the requirement to measure the volume change of the miniature sample with high
280 precision and resolution. The volumetric strain is determined based on image processing and
281 analysis of the CT images at each scan of the sample.

282 Using the synchrotron radiation facility, a raw 3D CT image of the sample at each scan is
283 acquired. Fig. 10 shows vertical slices of the sample at different scans, and indicates the increase
284 of voids in the sample at large shear strains (i.e., from 4.94% to 15.34%).

285 To quantify the porosity and volumetric strain of the sample, the raw 3D CT image is put
286 through a series of image processing and analysis. For illustration, Figs. 11(a)-(f) present the
287 image processing of a 2D horizontal slice to determine the porosity of the LBS sample. Please
288 note that the image processing is performed on 3D images in this study. First, an anisotropic
289 diffusion filter [44, 45] is applied to the raw CT image shown in Fig. 11(a) to remove random
290 noise within it. The anisotropic diffusion filter has the advantage of removing noise from
291 features and backgrounds of the image while preserving the boundaries and enhancing the
292 contrast between them. This is achieved by setting a diffusion stop threshold [45], which is
293 determined by a parametric study. Each voxel in the image is diffused unless the intensity

294 difference between the voxel and its six face-centered neighboring voxels exceeds the threshold
295 value. The resulting image is a grey-scale image shown in Fig. 11(b). Fig. 12 shows the intensity
296 histograms of the raw CT image and filtered CT image, respectively. The filtered CT image
297 shows a higher contrast between grains and air voids than the raw CT image, as seen in Fig. 12.
298 Subsequently, a global threshold (see Fig. 12) is applied to the smoothed grey-scale image to
299 transform it into a binary image shown in Fig. 11(c), where voxel intensities are either 1 or 0.

300 Based on the binary image, the volume of the solid phase (i.e., the sand grains) V_s is calculated
301 as the number of voxels with an intensity value of 1 multiplied by the voxel size (i.e., 6.5 μm^3).
302 Meanwhile, the sample volume V_T is also determined by implementing a series of morphological
303 operations on the binary image according to a method used by Andò [31]. Specifically, 12
304 episodes of image dilation are firstly implemented to the binary image to acquire another binary
305 image (i.e., the image shown in Fig. 11(d)), which contains a connected solid phase region. This
306 is followed by a 'filling hole' operation which replaces all the void phase voxels (i.e., the voxels
307 with an intensity value of 0) within the sample region with solid phase voxels (i.e., the voxels
308 with an intensity value of 1), as shown in Fig. 11(e). Note that while the image dilation decreases
309 the void phase within the sample region, the sample region itself is enlarged (i.e., the sample
310 boundary moves outwards). To alleviate this effect, 12 episodes of image erosion are applied
311 after the 'filling hole' operation. The final resulting image shown in Fig. 11(f) is used to
312 calculate the sample volume similar to the calculation of V_s. The morphological operation
313 process may have a tiny influence on the sample boundary shape because of the irreversibility of
314 the dilation and erosion operations. However, its influence on the sample volume results is
315 considered to be negligible due to the much larger number of voxels within the sample than on
316 its boundary. The sample porosity ϕ and volumetric strain ε_v are calculated as $\phi = \frac{V_T - V_S}{V_T}$ and

317 $\varepsilon_v = \frac{\Delta V_T}{V_T}$ (i.e., the decrease of the sample volume during a shear increment divided by the
318 original sample volume), respectively. Note that a positive volumetric strain denotes
319 compression.

320 To study the porosity distribution evolution, the local porosities of the sample (i.e., the local
321 porosities around individual particles) are calculated based on a distance transformation method
322 [46, 47]. Figs. 13(a)-(f) illustrate the image processing process of a horizontal CT slice to
323 determine the local porosities. In the binary image shown in Fig. 11(c), different particles
324 generally contact each other, so a watershed algorithm [48] is applied to separate the attached
325 particles prior to the calculation of local porosities. To this end, a distance transformation is first
326 implemented on the inverted binary image to obtain a distance map, before the watershed
327 algorithm is applied on the inverted distance map to separate the attached particles. Over-
328 segmentation sometimes occurs if the watershed algorithm is directly implemented because of
329 the intensity variations within the distance map [49]. A marker-based approach used in previous
330 studies [42, 50] is adopted to control the over-segmentation. The resulting image is a binary
331 image of separated particles shown in Fig. 13(a). Note that the regions with different colors in
332 the image denote different particles. To determine the local porosity around a particle, the
333 particle should be firstly extracted and stored in a binary image (Fig. 13(b)). Then, a distance
334 transformation is implemented to the binary image of separated particles (Fig. 13(a)) and the
335 binary image of the extracted particle (Fig. 13(b)), respectively. The resulting images are the two
336 images shown in Figs. 13(c) and 13(d), respectively. The local void region of the extracted
337 particle shown in Fig. 13(e) is determined as the region of pixels having an intensity value of 0 in
338 the resulting image of subtraction of the two distance transformation images (i.e., Figs. 13(c) and
339 13(d)). Fig. 13(f) shows the local void region of the extracted particle superimposed on the

binary image of separated particles. The local porosity p_i around a particle i is calculated by $p_i = \frac{V_R - V_P}{V_R}$ (where V_P and V_R are the volumes of particle i and the local void region of particle i, respectively). Note that the volumetric strain of the sample during each shear increment can also be determined according to the distance transformation method (i.e., $\varepsilon_v = \frac{\Delta \sum V_R}{\sum V_R}$). For comparison, the volumetric strain of the sample calculated using both methods is presented in Fig. 14, indicating that the two methods provide consistent volumetric strain results.

Meanwhile, particle kinematics (i.e., particle translation and particle rotation) of the sample during each shear increment are also quantitatively investigated through a particle-tracking approach [50], which uses either particle volume or particle surface area as a particle-tracking criterion to track individual particles within the sample. The centroid coordinates and orientations of tracked particles in CT images from different scans are used to determine their displacements and rotations, respectively. Specifically, a particle motion is decomposed into a translation of the particle mass center and a rotation around a certain axis passing through the mass center. The particle translation (i.e., particle displacement) is calculated as the difference of the particle centroid coordinates at the end and the start of the shear increment. The particle rotation is calculated according a rotation matrix, which is determined based on the orientation matrices of the particle at the end and the start of the shear increment. The readers are referred to literature [50] for the full description of the calculation of particle translation and particle rotation. Additionally, by combing the particle tracking results with the determination of local porosities, the volumetric strain distribution of the sample during each shear increment is investigated. This is achieved by calculating local volumetric strain around each particle, i.e., the volumetric strain of the local void region of the particle. For each shear increment, the local

volumetric strain ε_{v_i} of a particle i is determined by the volume change of local void region of the particle during the shear increment (i.e., $\varepsilon_{v_i} = \frac{V_R' - V_R}{V_R}$, where V_R and V_R' are the volume of local void region at the start and the end of the shear increment, respectively). The authors have checked the reliability of the quantification of volumetric strains in this study. It is found that the presented method provides strain results basically consistent with those from a grid-based strain calculation method [51]. The grid-based method calculates volumetric strains of the sample at a shear increment based on particle translations and rotations during the shear increment. In the method, a grid-type discretization is employed over the sample space, in which each grid is associated to a particle based on a criterion. The displacement of each grid is determined according to the kinematics of its associated particle. The grid displacements are used for the strain calculation.

Fig. 15 shows a vertical slice of local porosity distributions of the sample at different axial strains. Note that only the porosities at the particles' centroids are calculated, and a linear interpolation is adopted for the porosities between any two particle centroids. As shown in Fig. 15, the sample shows a slightly inhomogeneous porosity distribution at the isotropic state (i.e., the axial strain of 0%) and the axial strain of 0.98%. Particles with large local porosities are disorganized in the sample, and this inhomogeneity increases as the deviatoric stress approaches the peak around the axial strain of 4.94%. The sample exhibits several zones of high porosity in the center. In the post-peak shear stage (i.e., axial strains of 10.40% and 15.34%), a localized band of high porosity is well developed. Overall, the sample experiences an increase of local porosities during the shear from the axial strain of 0.98% to 15.34%.

Fig. 16 shows the normalized frequency distributions of local porosity of the sample at different axial strains, and presents the mean value and the standard deviation. From Fig. 16 we can see that from the axial strain of 0% to 0.98%, there is no obvious change of the normalized frequency distribution. From the axial strain of 0.98% to 15.34%, the normalized frequency of particles with high local porosities (e.g., local porosities larger than 0.5) increases, while that with low local porosities (e.g., local porosities smaller than 0.4) decreases. This results in the increase of the mean local porosity value, which indicates a volumetric dilation, during the shear stage. Meanwhile, the standard deviation of local porosity – which reflects the homogeneity of the sample (the sample is completely homogenous when the standard deviation is 0, i.e., all particles have the same porosity) – also experiences an increase during the shear stage, from 0.98% to 15.34%. This indicates that the sample becomes increasingly inhomogeneous in the volumetric dilation process.

Figs. 17(a)-(d) show the particle displacement and particle rotation of the sample at different axial strain increments. Note that the rotation magnitudes of particles shown in Fig. 17 are the rotation angles of the particles around their own rotation axes. The rotation axis of a particle is determined according to the particle rotation matrix, which is different for different particles. At the early stage of shear (i.e., 0~0.98%) shown in Fig. 17(a), there is no obvious localization of particle displacement (left), or particle rotation (right) occurring within the sample. At the axial strain increment of 4.94~10.40%, the sample experiences clearly localized particle displacement and particle rotation, as shown in Fig. 17(c). Eventually, the sample fails along a well-defined localized displacement band shown in Fig. 17(d). Figs. 18(a)-(d) show volumetric strain distributions of the sample at different shear increments, in which both 3D maps and vertical slices of the volumetric strains are displayed. Note that negative values denote dilation. The

406 sample exhibits no distinct localization of volumetric strain at the early stage of shear, but
407 experiences a strong localized dilation in the post peak stage of shear (i.e., 4.94~15.34%), which
408 is similar to the evolution of particle kinematics.

409 **5 Conclusions**

410 A miniature apparatus is specially fabricated and used for experimental investigation of the
411 micro-scale mechanical behavior of granular soils under triaxial shear. The apparatus is similar
412 to the conventional triaxial apparatus from a structural point of view, and can be used in
413 conjunction with X-ray μCT for in-situ testing. The detailed design of this apparatus is presented.

414 An experiment of an LBS sample sheared under a confining stress of 500 kPa is demonstrated.
415 The micro-scale characteristic changes of the sample (e.g., the evolutions of local porosities,
416 particle kinematics and volumetric strain distribution), which are otherwise not possible to
417 examine by conventional triaxial tests, are quantitatively studied using image processing and
418 analysis techniques. A novel method is presented to quantify the volumetric strain distribution of
419 the sample throughout the test.

420 The volumetric strains are calculated using two image processing-based methods, which are
421 found to provide consistent results. The sample shows a slight inhomogeneity of local porosities
422 and no apparent localization of particle kinematics or volumetric strain in the early stage of
423 shearing, with high-porosity particles disorganized in the sample. An obvious inhomogeneity of
424 local porosities and a slight localization of particle kinematics and volumetric strain are observed
425 in the middle of the sample around the peak of the deviatoric stress. A localized band of high
426 porosities, particle kinematics and volumetric strain is gradually developed in the sample at the
427 post-peak shear stage.

The miniature triaxial apparatus, in conjunction with X-ray μCT and advanced image processing and analysis techniques, has provided an effective way to unravel the micromechanical mechanism of the failure of granular soils subjected to loading.

Acknowledgement

This study was supported by the General Research Fund No. CityU 11272916 from the Research Grant Council of the Hong Kong SAR, Research Grant No. 51779213 from the National Science Foundation of China, the open-research grant No. SLDRCE15-04 from State Key Laboratory of Civil Engineering Disaster Prevention of Tongji University, and the BL13W beam-line of Shanghai Synchrotron Radiation Facility (SSRF). The authors would like to thank Dr. Edward Andò in Université Grenoble Alpes for providing his PhD thesis.

References

1. Lee KL, Farhoomand I (1967) Compressibility and crushing of granular soil in anisotropic triaxial compression. Canadian Geotechnical Journal 4(1): 68-86.

2. Fragaszy RJ, Voss ME (1986) Undrained compression behavior of sand. Journal of geotechnical engineering 112(3): 334-347.

3. Arshad MI, Tehrani FS, Prezzi M, Salgado R (2014) Experimental study of cone penetration in silica sand using digital image correlation. Géotechnique 64(7): 551-569.

4. Wang J, Yan H (2012) DEM analysis of energy dissipation in crushable soils. Soils and Foundations 52(4): 644-657.

5. Wang J, Yan H (2013) On the role of particle crushing in the shear failure behavior of granular soils by DEM. International Journal for Numerical and Analytical Methods in Geomechanics 37(8): 832-854.

6. Coop MR, Sorensen KK, Freitas TB, Georgoutsos G (2004) Particle crushing during shearing of a carbonate sand. Géotechnique 54(3): 157-163.

452 7. Cavarretta I, Coop MR, O'Sullivan C (2010) The influence of particle characteristics on the
453 behaviour of coarse grained soils. Géotechnique 60(6): 413-423

454 8. Senetakis K, Coop MR (2015) Micro-mechanical experimental investigation of grain-to-grain
455 sliding stiffness of quartz minerals. Experimental Mechanics 55(6): 1187-1190.

456 9. Cundall PA, Strack OD (1979) A discrete numerical model for granular assemblies.
457 Géotechnique 29(1): 47-65.

458 10. Iwashita K, Oda M (1998) Rolling resistance at contacts in simulation of shear band
459 development by DEM. Journal of engineering mechanics 124(3): 285-292.

460 11. Jiang MJ, Yu HS, Harris D (2005) A novel discrete model for granular material incorporating
461 rolling resistance. Computers and Geotechnics 32(5): 340-357.

462 12. Zhou B, Huang R, Wang H, Wang J (2013) DEM investigation of particle anti-rotation
463 effects on the micromechanical response of granular materials. Granular Matter 15(3): 315-326.

464 13. Matsushima T, Saomoto H (2002) Discrete element modeling for irregularly-shaped sand
465 grains. Proc. NUMGE2002: Numerical Methods in Geotechnical Engineering, pp 239-246.

466 14. Price M, Murariu V, Morrison G (2007) Sphere clump generation and trajectory comparison
467 for real particles. Proceedings of Discrete Element Modelling, pp 2007.

468 15. Ferellec J, McDowell G (2010) Modelling realistic shape and particle inertia in DEM.
469 Géotechnique 60(3): 227-232.

470 16. Ng TT (1999) Fabric study of granular materials after compaction. Journal of engineering
471 mechanics 125(12): 1390-1394.

472 17. Cleary PW (2008) The effect of particle shape on simple shear flows. Powder Technology
473 179(3): 144-163.

474 18. Oda M (1972) Initial fabrics and their relations to mechanical properties of granular material.
475 Soils and foundations 12(1): 17-36.

476 19. Konagai K, Tamura C, Rangelow P, Matsushima T (1992) Laser-aided tomography: a tool
477 for visualization of changes in the fabric of granular assemblage. Structural
478 Engineering/Earthquake Engineering 9(3): 193s-201s.

20. Johns RA, Steude JS, Castanier LM, Roberts PV (1993) Nondestructive measurements of fracture aperture in crystalline rock cores using X ray computed tomography. Journal of Geophysical Research: Solid Earth 98(B2): 1889-900.

21. Ohtani T, Nakano T, Nakashima Y, Muraoka H (2001) Three-dimensional shape analysis of miarolitic cavities and enclaves in the Kakkonda granite by X-ray computed tomography. Journal of Structural Geology 23(11): 1741-51.

22. Oda M, Takemura T, Takahashi M (2004) Microstructure in shear band observed by microfocus X-ray computed tomography. Géotechnique 54(8): 539-542.

23. Fonseca J, O'Sullivan C, Coop MR, Lee PD (2013) Quantifying the evolution of soil fabric during shearing using directional parameters. Géotechnique 63(6): 487-499.

24. Fonseca J, O'Sullivan C, Coop MR, Lee PD (2013) Quantifying the evolution of soil fabric during shearing using scalar parameters. Géotechnique 63(10): 818-829.

25. Desrues J, Chambon R, Mokni M, Mazerolle F (1996) Void ratio evolution inside shear bands in triaxial sand specimens studied by computed tomography. Géotechnique 46(3): 529-46.

26. Lenoir N, Bornert M, Desrues J, Bésuelle P, Viggiani G (2007) Volumetric digital image correlation applied to X-ray micro tomography images from triaxial compression tests on argillaceous rock. Strain 43(3): 193-205.

27. Watanabe Y, Lenoir N, Otani J, Nakai T (2012) Displacement in sand under triaxial compression by tracking soil particles on X-ray CT data. Soils and foundations 52(2): 312-320.

28. Matsushima T, Katagiri J, Uesugi K, Nakano T, Tsuchiyama A (2006) Micro X-ray CT at Spring-8 for granular mechanics. In Soil Stress-Strain Behavior: Measurement, Modeling and Analysis: A Collection of Papers of the Geotechnical Symposium in Rome 146: 225-234.

29. Otani J, Mukunoki T, Obara Y (2002) Characterization of failure in sand under triaxial compression using an industrial X-ray CT scanner. International Journal of Physical Modelling in Geotechnics 2(1): 15-22.

30. Hasan A, Alshibli K (2012) Three dimensional fabric evolution of sheared sand. Granular Matter 14(4): 469-482.

31. Andò E (2013) Étude experimentale de l'évolution de la microstructure d'un milieu granulaire sous chargement mécanique a l'aide de la tomographie rayons x PhD Thesis, Docteur de L'Université de Grenoble.

509 32. Higo Y, Oka F, Sato T, Matsushima Y, Kimoto S (2013) Investigation of localized
510 deformation in partially saturated sand under triaxial compression using microfocus X-ray CT
511 with digital image correlation. Soils and Foundations 53(2): 181-198.

512 33. Higo Y, Oka F, Kimoto S, Sanagawa T, Matsushima Y (2011) Study of strain localization
513 and microstructural changes in partially saturated sand during triaxial tests using microfocus X-
514 ray CT. Soils and foundations 51(1): 95-111.

515 34. Head KH (1982) Manual of soil laboratory testing. Vol. 2. Pentech Press Ltd., London.

516 35. Indraratna B, Wijewardena LSS, Balasubramaniam AS (1993) Large-scale triaxial testing of
517 greywacke rockfill. Géotechnique 43(1): 37-51.

518 36. Wang J, Gutierrez M (2010) Discrete element simulations of direct shear specimen scale
519 effects. Géotechnique 60(5): 395-409.

520 37. Desrues J, Andò E, Mevoli FA, Debove L, Viggiani G (2018) How does strain localise in
521 standard triaxial tests on sand: Revisiting the mechanism 20 years on. Mechanics Research
522 Communications 92: 142-146.

523 38. Hall SA, Bornert M, Desrues J, Pannier Y, Lenoir N, Viggiani G, Bésuelle P (2010) Discrete
524 and continuum analysis of localised deformation in sand using X-ray μCT and volumetric digital
525 image correlation. Géotechnique 60(5): 315-322.

526 39. Andò E, Viggiani G, Hall SA, Desrues J (2013) Experimental micro-mechanics of granular
527 media studied by x-ray tomography: recent results and challenges. Géotechnique Letters 3 (3):
528 142-146.

529 40. Vlahinić I, Kawamoto R, Andò E, Viggiani G, Andrade JE (2017) From computed
530 tomography to mechanics of granular materials via level set bridge. Acta Geotechnica 12: 85-95.

531 41. Cheng Z, Wang J (2018) Experimental investigation of inter-particle contact evolution of
532 sheared granular materials using X-ray micro-tomography. Soils and Foundations.
533 https://doi.org/10.1016/j.sandf.2018.08.008

534 42. Zhao BD, Wang JF, Coop MR, Viggiani G, Jiang MJ (2015) An investigation of single sand
535 particle fracture using X-ray micro-tomography. Géotechnique 65(8): 625-641.

536 43. Wang WY, Coop MR (2016) An investigation of breakage behaviour of single sand particles
537 using a high-speed microscope camera. Géotechnique 66(12): 984-998.

538 44. Perona P, Malik J (1990). Scale-space and edge detection using anisotropic diffusion. IEEE
539 Transactions on pattern analysis and machine intelligence 12(7): 629-639.

540 45. Bernard D, Guillon O, Combaret N, Plougonven E (2011). Constrained sintering of glass
541 films: Microstructure evolution assessed through synchrotron computed microtomography. Acta
542 Materialia 59(16): 6228-6238.

543 46. Al-Raoush R, Alshibli KA (2006) Distribution of local void ratio in porous media systems
544 from 3D X-ray microtomography images. Physica A: Statistical Mechanics and its Applications
545 361(2): 441-456

546 47. Cheng Z (2018) Investigation of the grain-scale mechanical behavior of granular soils under
547 shear using X-ray micro-tomography. PhD thesis, City University of Hong Kong.

548 48. Beucher S, Lantuejoul C (1979) Use of watersheds in contour detection. Proceedings of the
549 international workshop on image processing, real-time edge and motion detection/estimation,
550 Rennes, France.

551 49. Gonzalez RC, Woods RE (2010) Digital image processing. Upper Saddle River, NJ, USA:
552 Pearson/Prentice Hall.

553 50. Cheng Z, Wang J (2018) A particle-tracking method for experimental investigation of
554 kinematics of sand particles under triaxial compression. Powder Technology 328: 436-451.

555 51. Cheng Z, Wang J (2019) Quantification of the strain field of sands based on X-ray micro-
556 tomography: A comparison between a grid-based method and a mesh-based method. Powder
557 Technology 344: 314-334.

558

559 **List of Figures**

578 Fig. 13 Illustration of the image processing of a 2D horizontal slice to determine local porosities:
579 (a) a binary image of separated particles, (b) a binary image of an extracted particle, (c) distance
580 transformation of image (a), (d) distance transformation of image (b), (e) extracted local void
581 region, (f) the local void region superimposed on image (a)

582 Fig. 14 Comparison between the volumetric strains of the sample as calculated by two methods

583 Fig. 15 A vertical slice of local porosity distributions of the sample at different axial strains

584 Fig. 16 Normalized frequency distributions of local porosity of the sample at different axial
585 strains

586 Fig. 17 Particle displacement and rotation of the sample during the axial strain increments of (a)
587 0~0.98% (b) 0.98~4.94% (c) 4.94~10.40% (d) 10.40~15.34%

588 Fig. 18 Volumetric strain distributions of the sample during the axial strain increments of (a)
589 0~0.98% (b) 0.98~4.94% (c) 4.94~10.40% (d) 10.40~15.34%

590
591
592
593
594
595
596
597
598
599

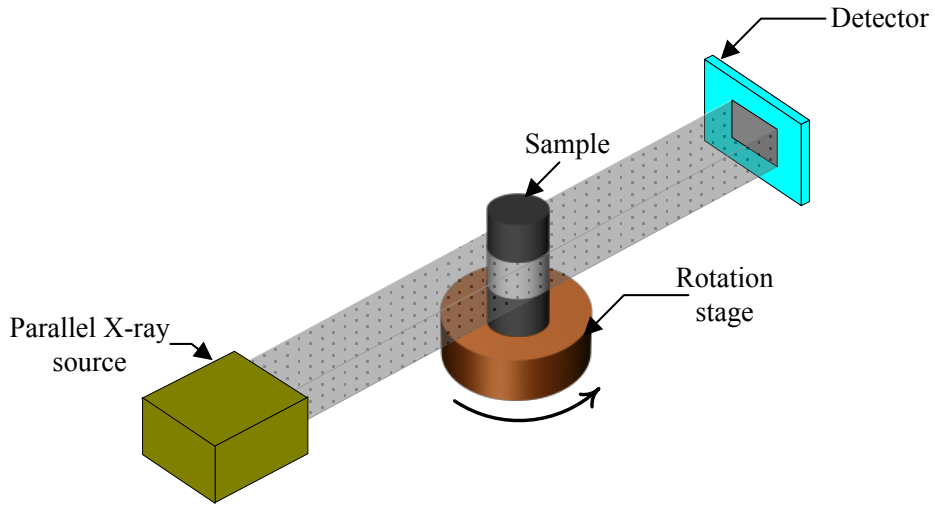

600

601 Fig. 1 Schematic of a typical parallel beam X-ray μCT facility

602

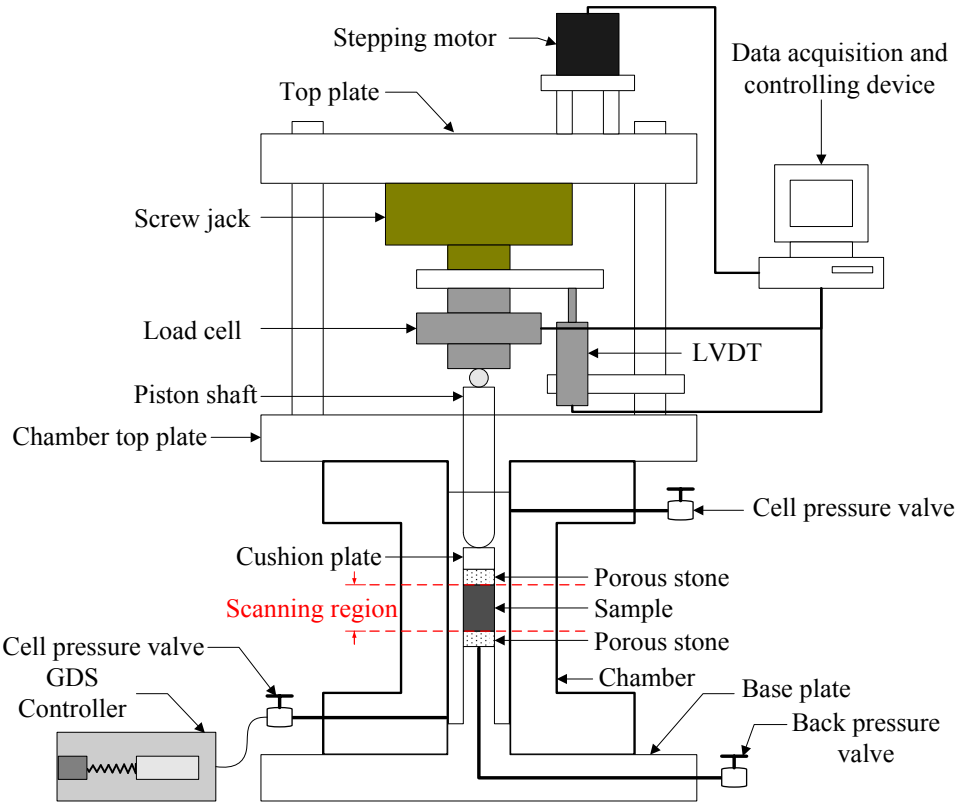

603

604 (a)

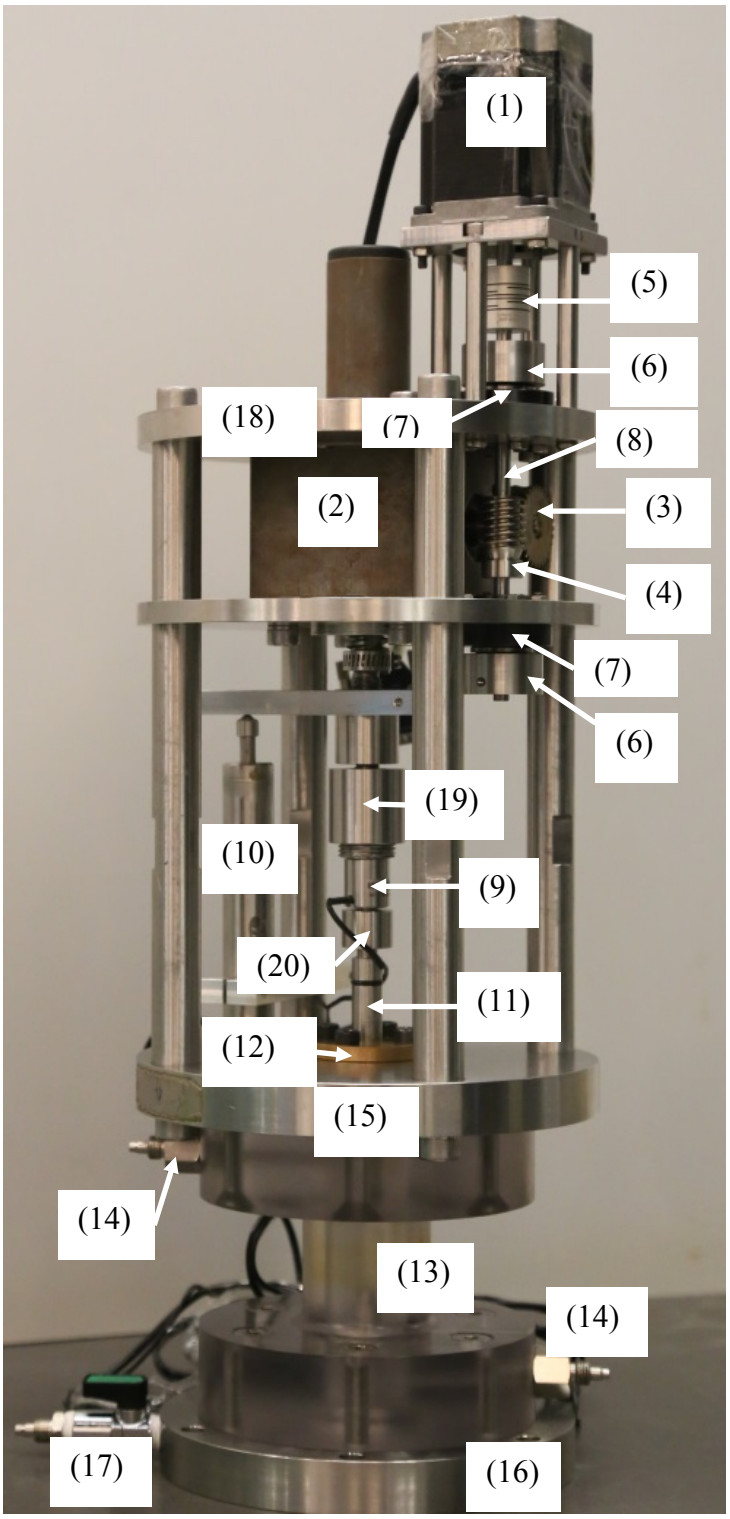

(1) Stepping motor

(2) Screw jack

(3) Worm gear

(4) Worm

(5) Motor coupling

(6) Axial thrust bearing

(7) Radial thrust bearing

(8) Worm shaft

(9) Load cell

(10) LVDT

(11) Piston shaft

(12) Piston shaft sleeve

(13) Chamber

(14) Cell pressure valve

(15) Chamber top plate

(16) Base plate

(17) Back pressure valve

(18) Top plate

(19) and (20) Screw adaptors

(b)

Fig. 2 The triaxial system: (a) schematic of the triaxial system, (b) photograph of the triaxial apparatus

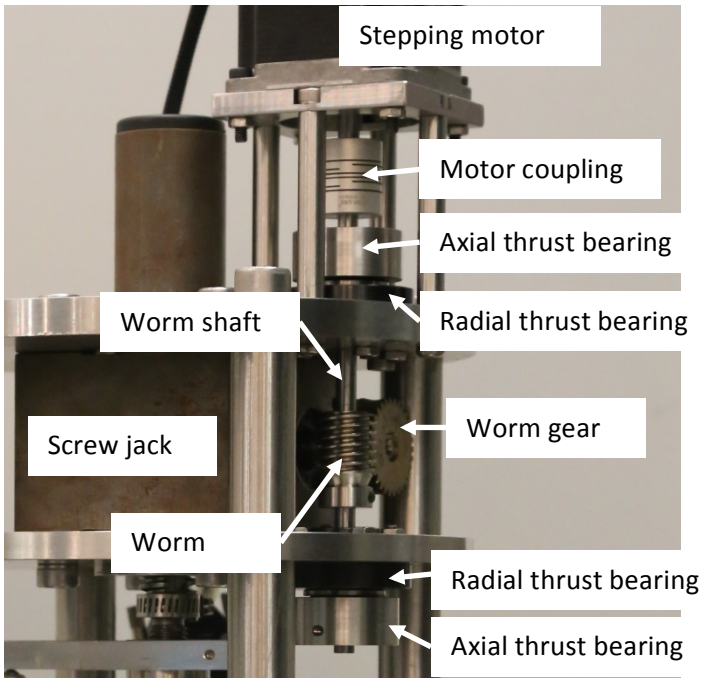

609

610 Fig. 3 A closer view of the axial loading device

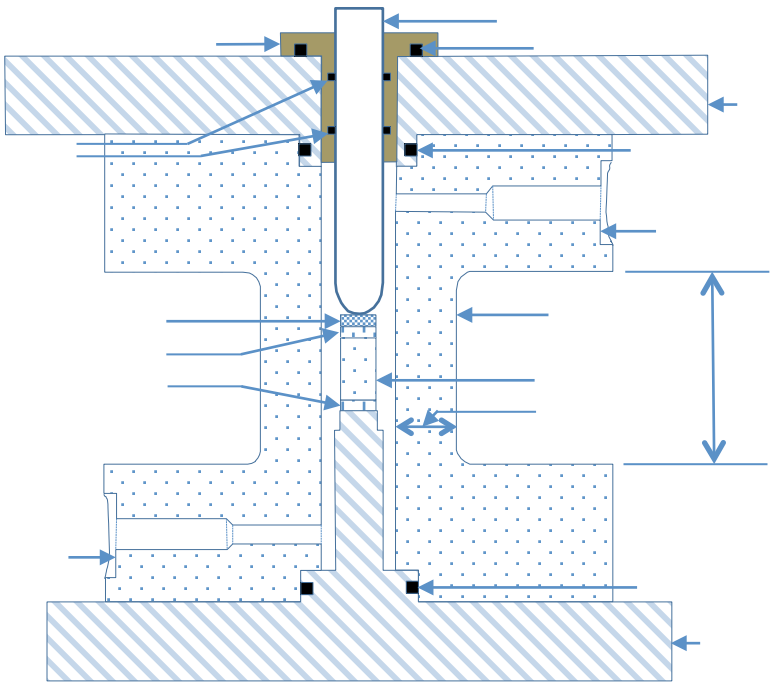

611

612 Fig. 4 A schematic of the seal design of the apparatus

613

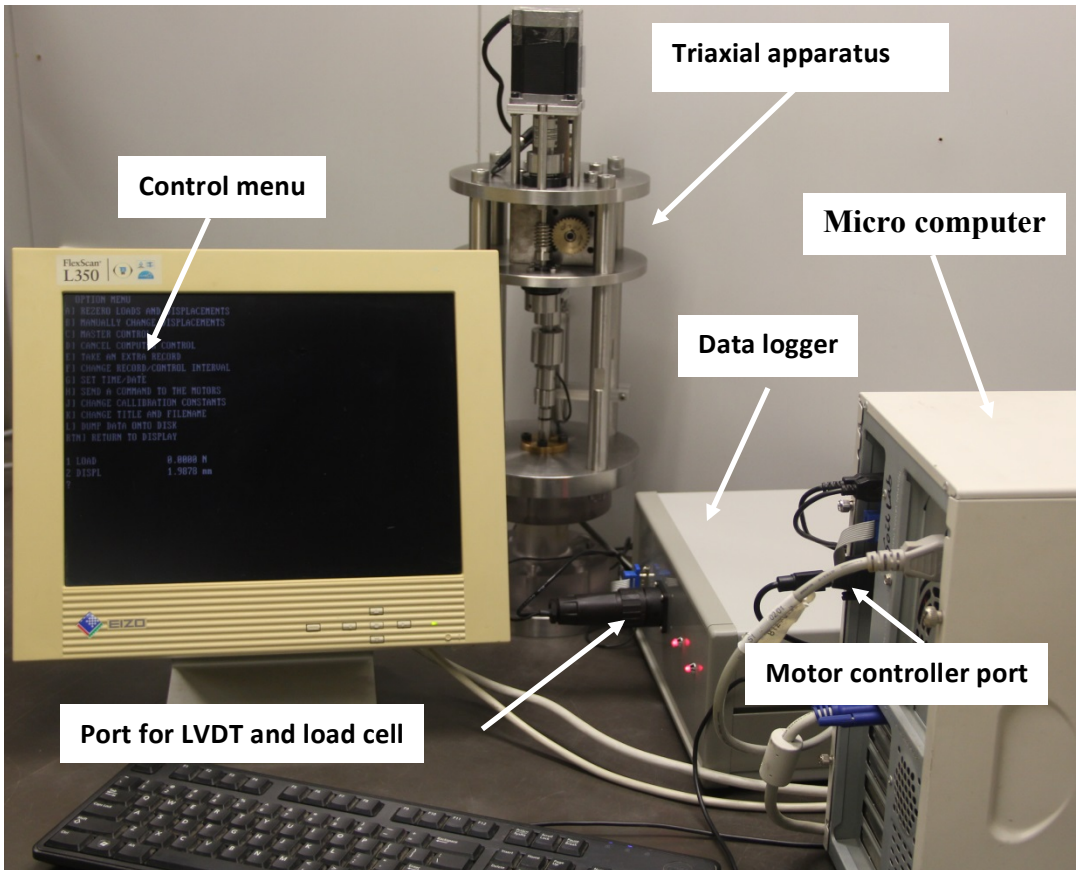

614

615 Fig. 5 Data acquisition and controlling system

616

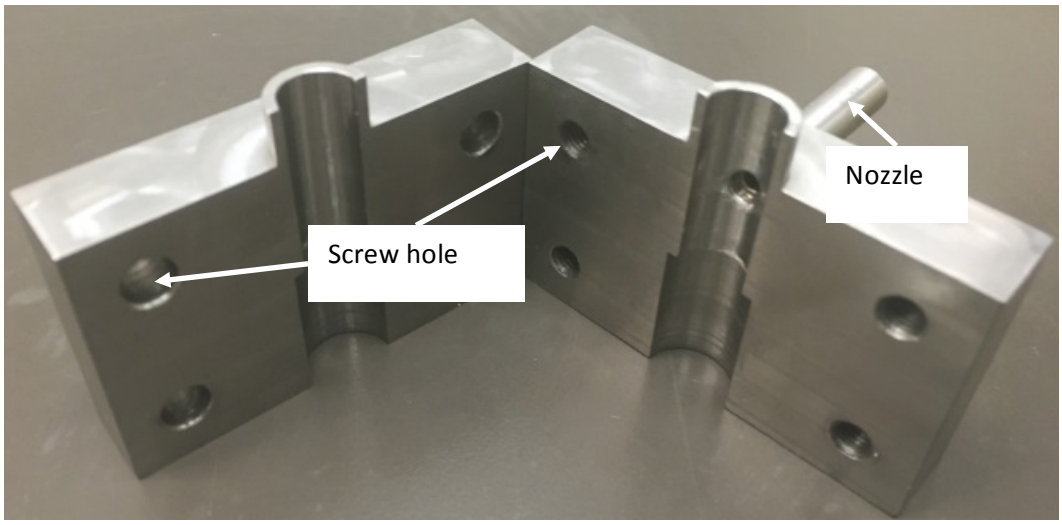

617

618 Fig. 6 Photograph of the sample maker

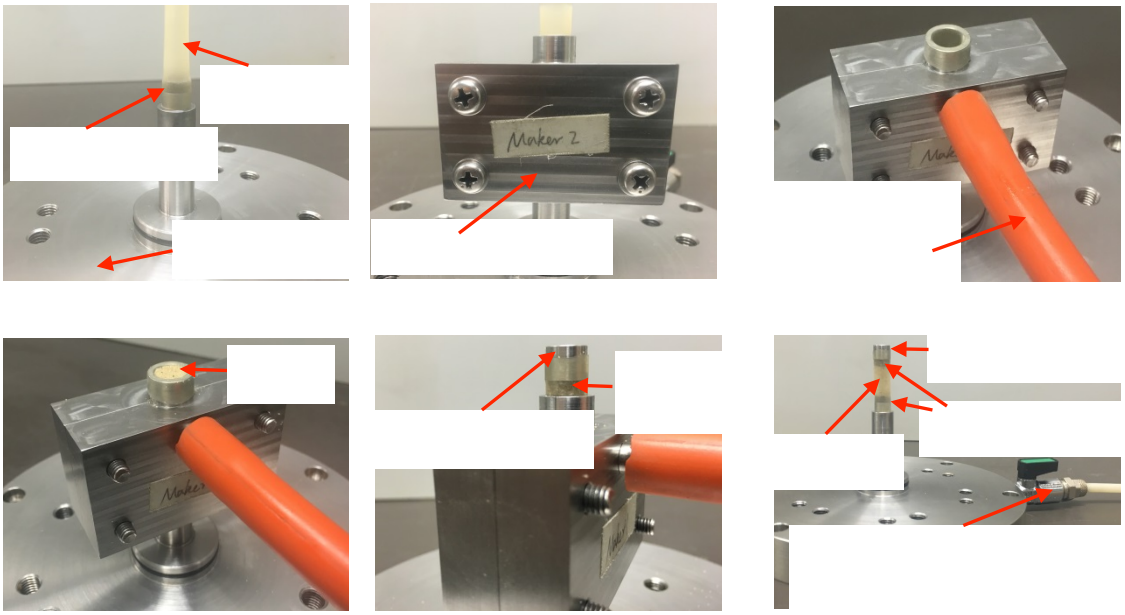

619

620 Fig. 7 The process of making a sample

621

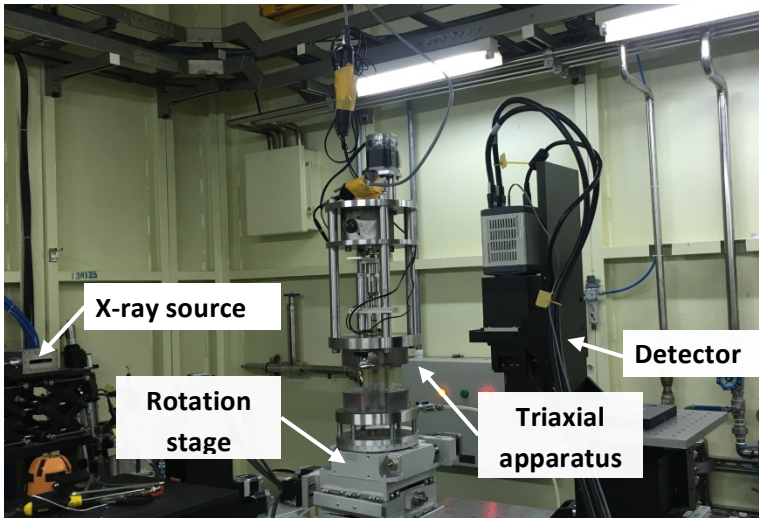

(a)

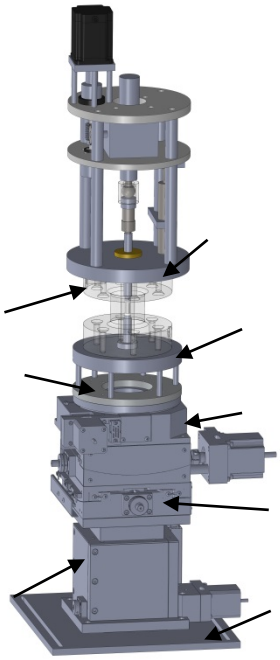

(b)

Fig. 8 The triaxial apparatus being used in conjunction with the synchrotron radiation facility: (a) a photograph, (b) a schematic of the connection between the apparatus and the synchrotron radiation facility.

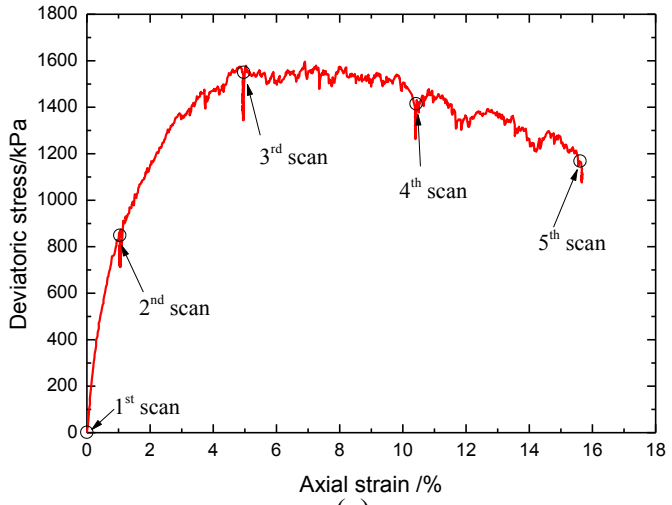

(a)

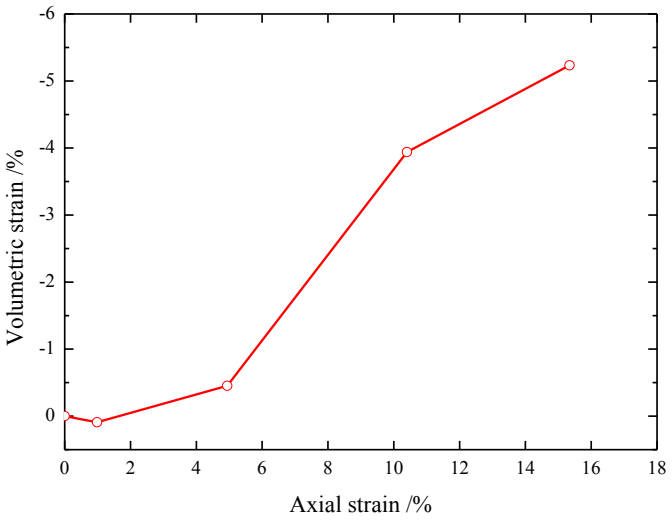

(b)

629

630 Fig. 9 Stress–strain curves of the LBS sample: (a) deviatoric stress vs. axial strain, (b) volumetric

631 strain vs. axial strain

632

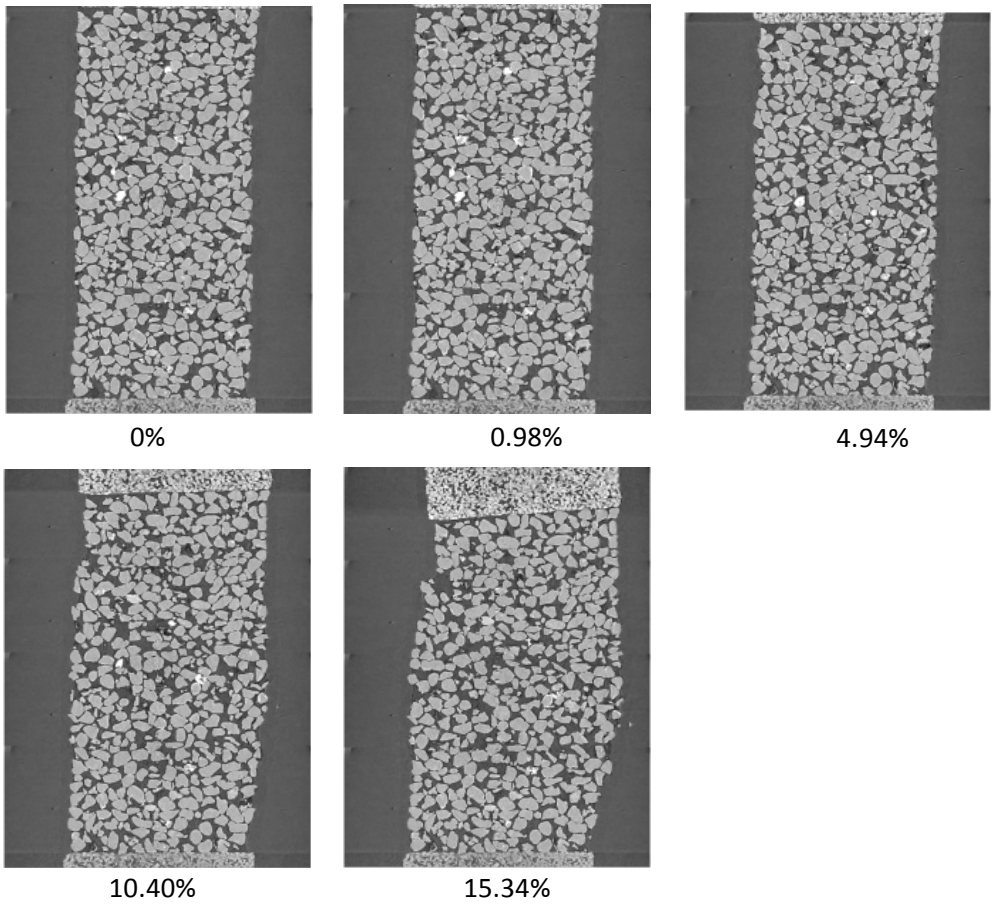

633

634 Fig. 10 Vertical slices of the sample at different scans

635

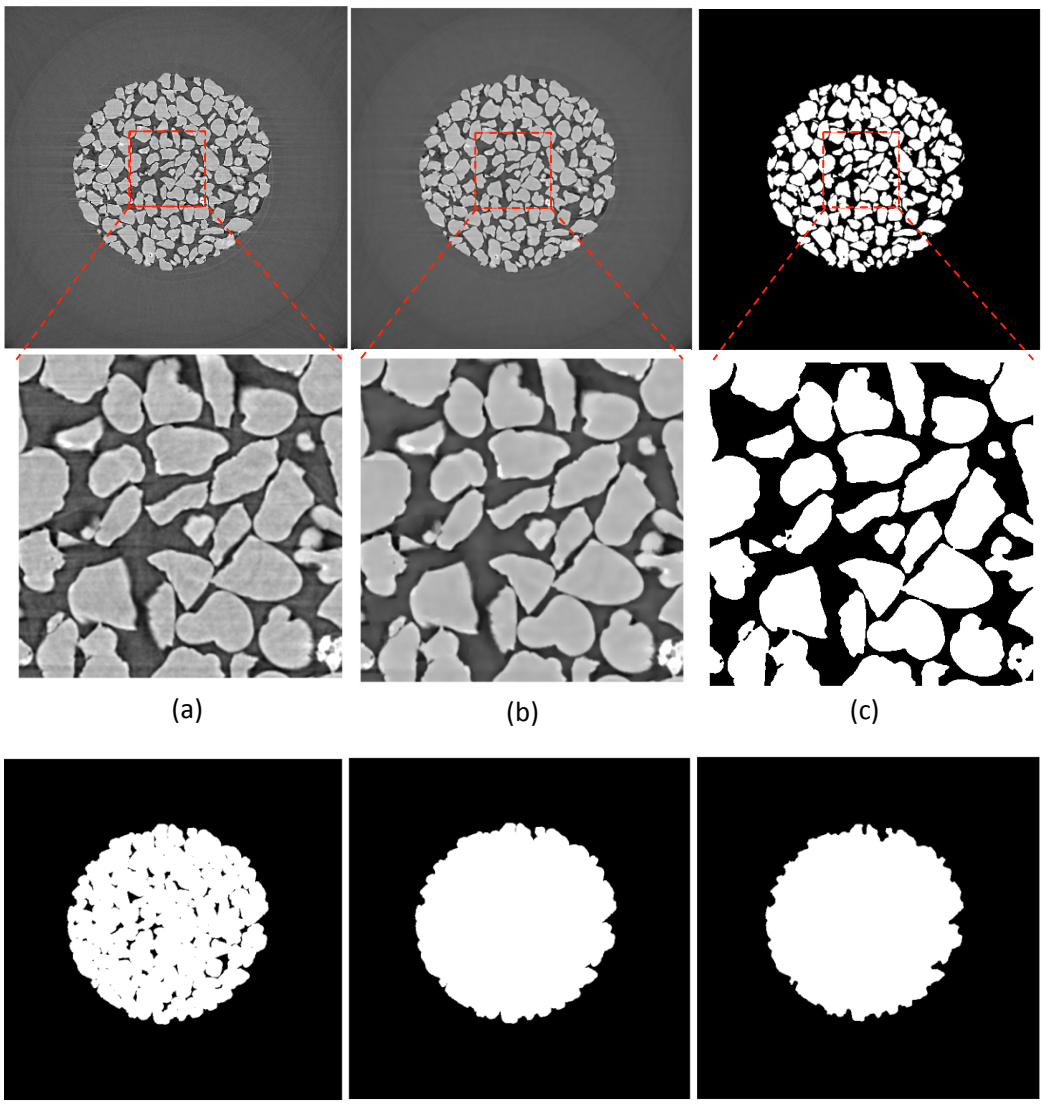

636

637 Fig. 11 Illustration of the image processing of a 2D horizontal slice to determine sample porosity:

638 (a) raw CT image, (b) filtered CT image, (c) binary image, (d) after 12 times of dilation of image

639 (c), (e) after filling holes of image (d), (f) after 12 times of erosion of image (e)

640

641

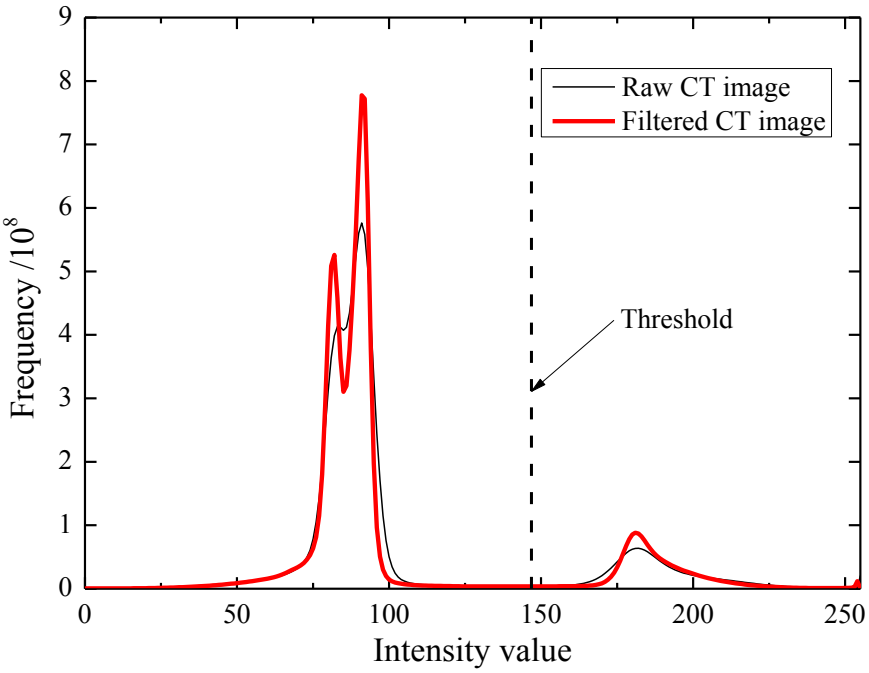

642

643 Fig. 12 Intensity histograms of the CT image before and after image filtering

644

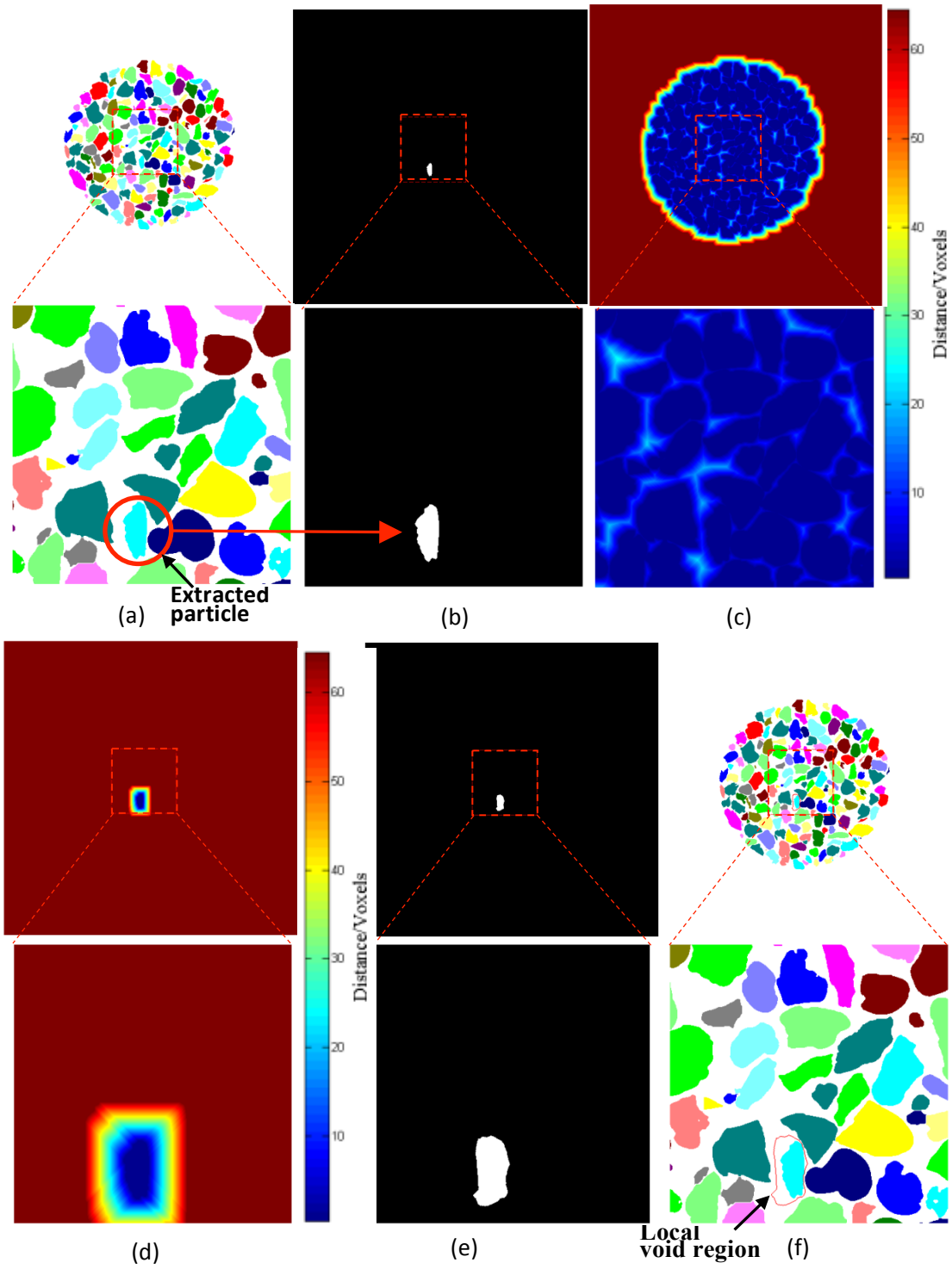

Fig. 13 Illustration of the image processing of a 2D horizontal slice to determine local porosities: (a) a binary image of separated particles, (b) a binary image of an extracted particle, (c) distance transformation of image (a), (d) distance transformation of image (b), (e) extracted local void region, (f) the local void region superimposed on image (a)

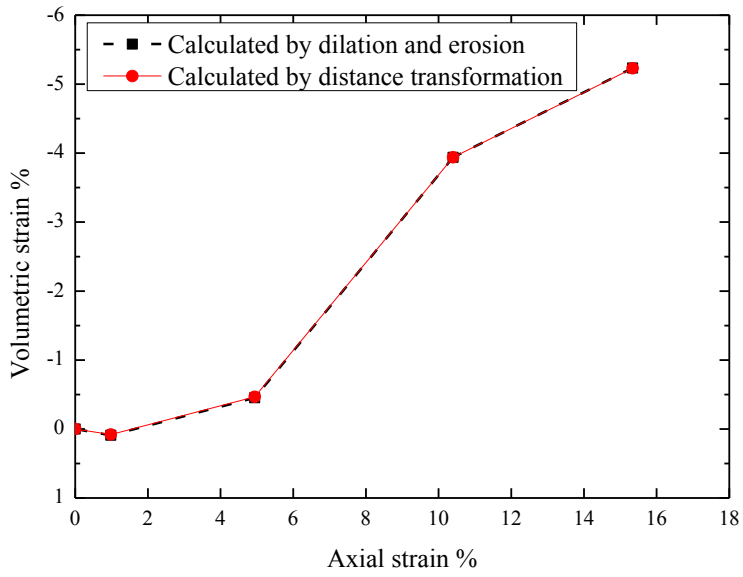

650

651 Fig. 14 Comparison between the volumetric strains of the sample as calculated by two methods

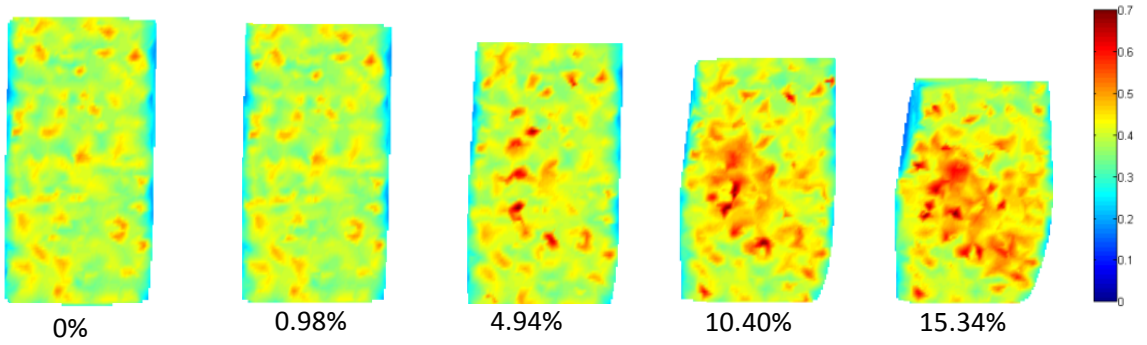

652

653 Fig. 15 A vertical slice of local porosity distributions of the sample at different axial strains

654

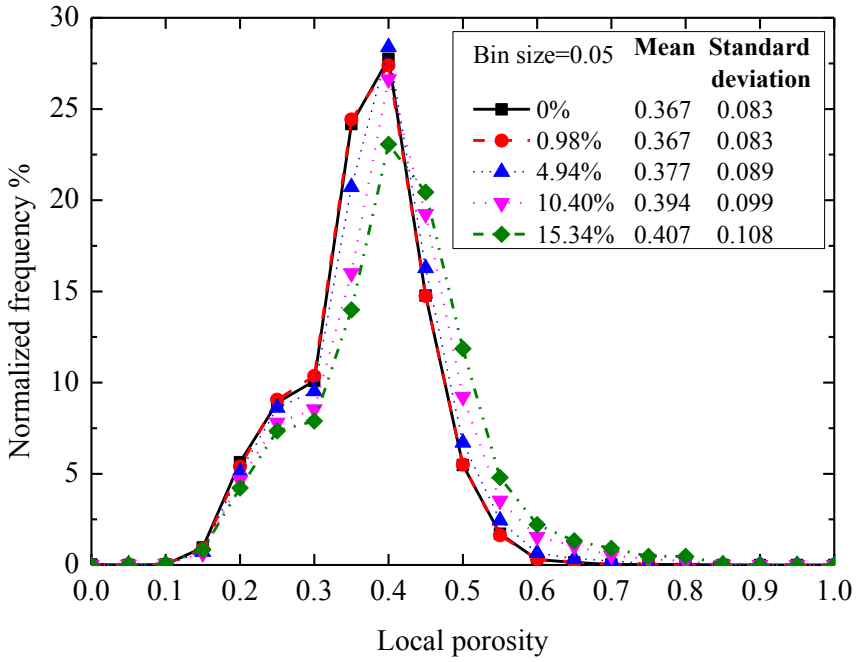

Fig. 16 Normalized frequency distributions of local porosity of the sample at different axial strains

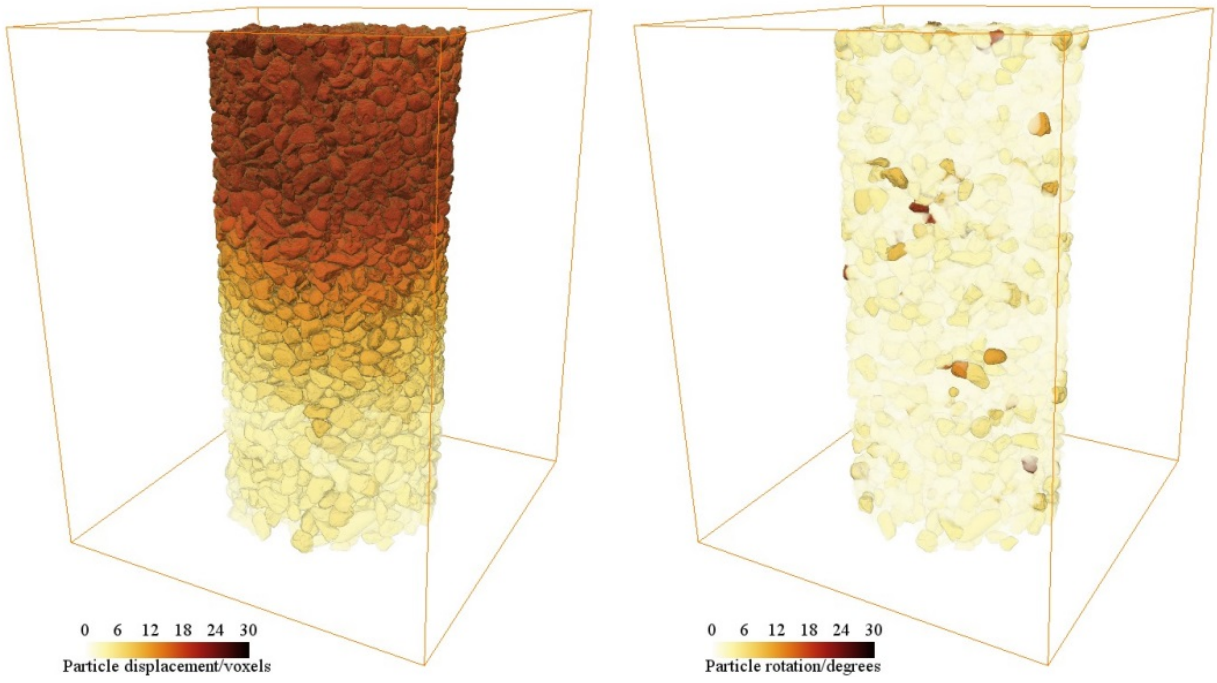
0 6 12 18 24 30
Particle displacement/voxels
0 6 12 18 24 30
Particle rotation/degrees

(a)

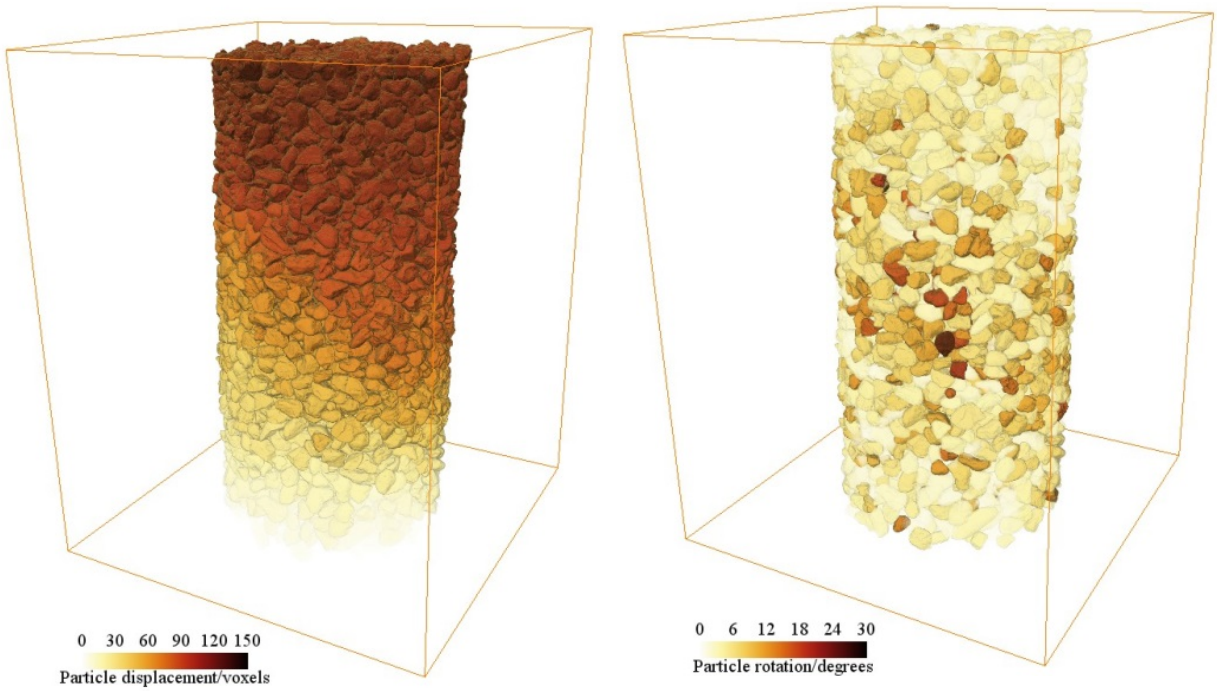
0 30 60 90 120 150
Particle displacement/voxels
0 6 12 18 24 30
Particle rotation/degrees

(b)

660

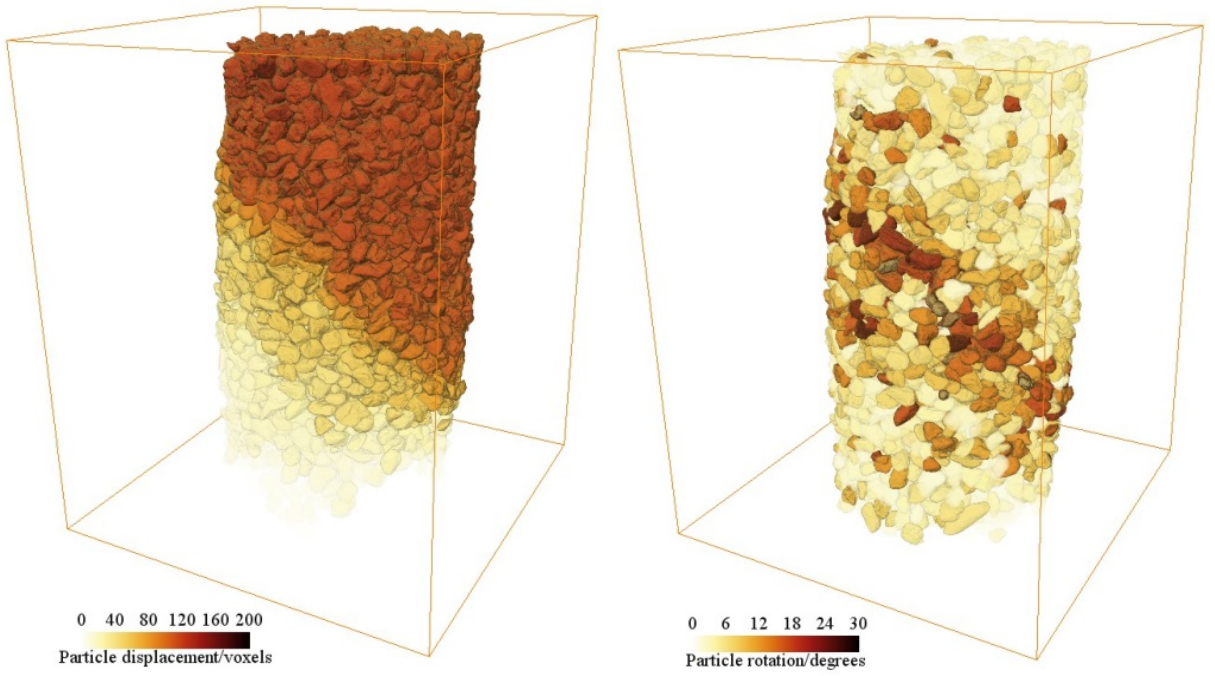

(c)

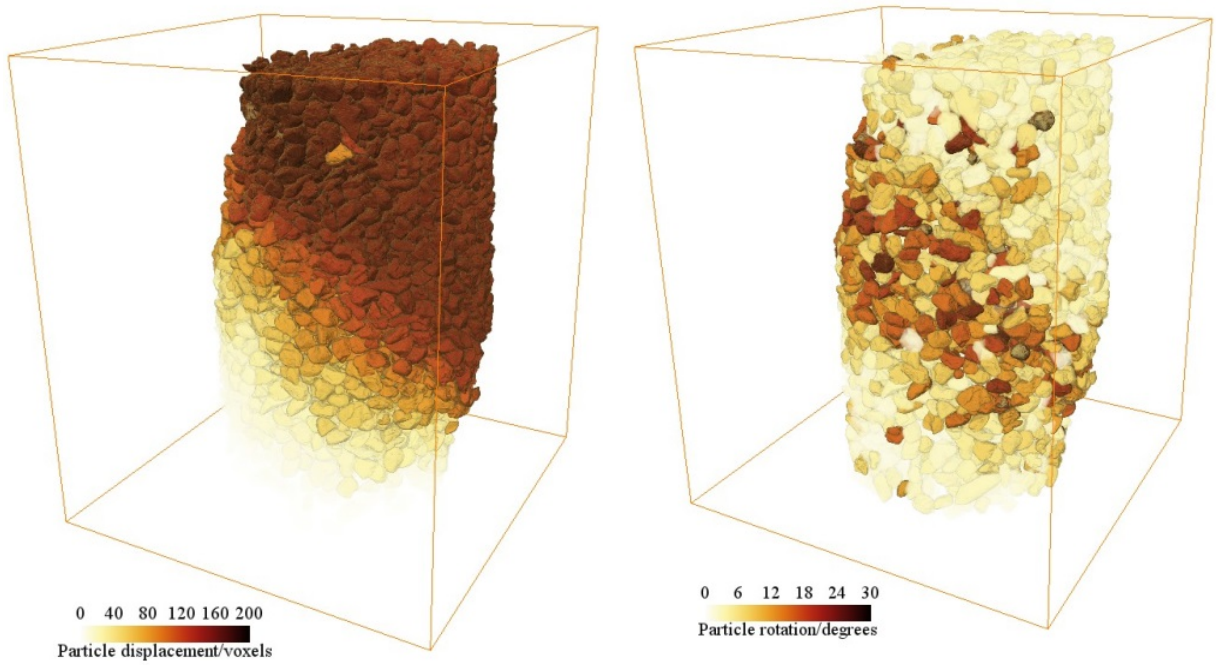

(d)

661

662 Fig. 17 Particle displacement and rotation of the sample during the axial strain increments of (a)

663 0~0.98% (b) 0.98~4.94% (c) 4.94~10.40% (d) 10.40~15.34%

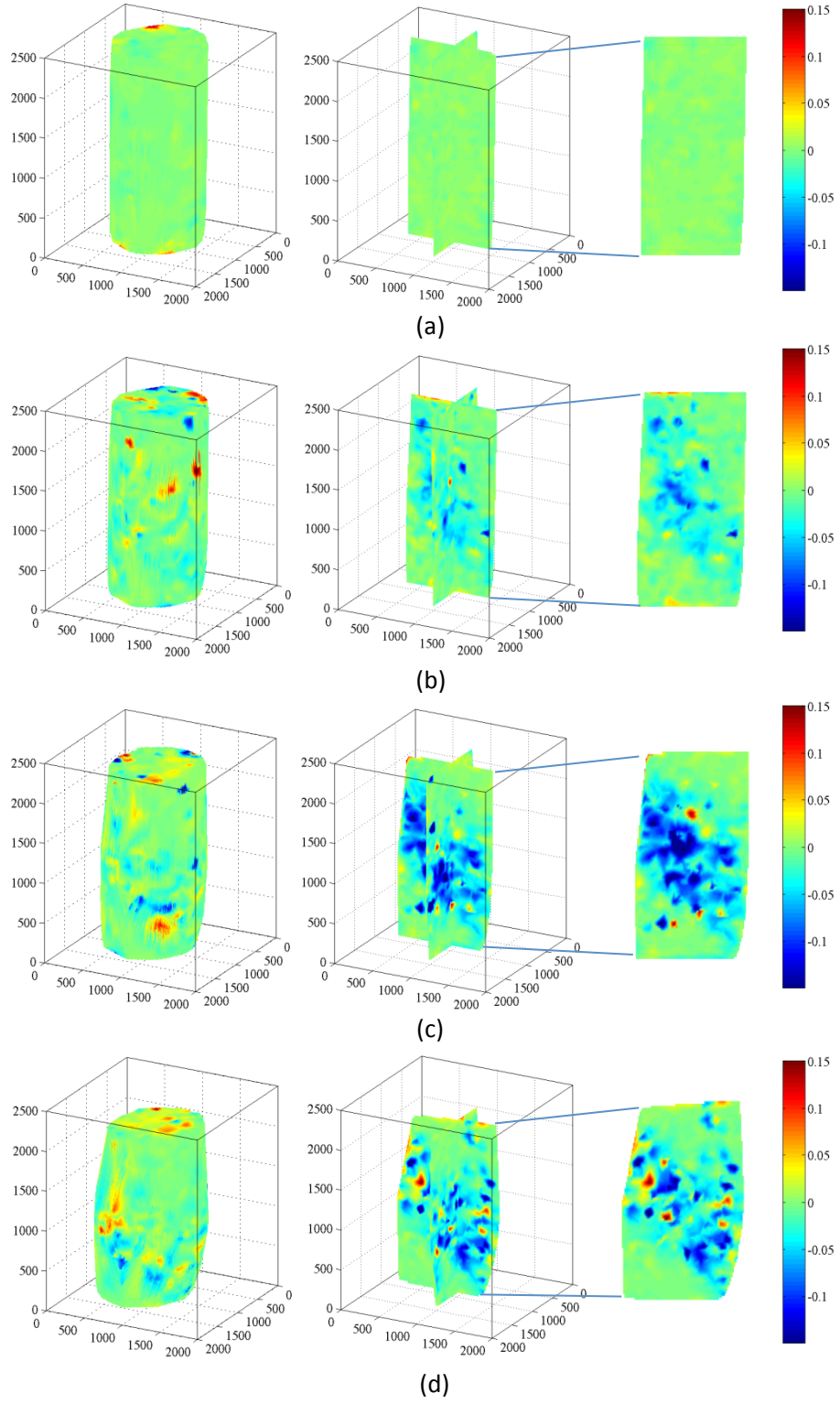

664

665 Fig. 18 Volumetric strain distributions of the sample during the axial strain increments of (a)

666 0~0.98% (b) 0.98~4.94% (c) 4.94~10.40% (d) 10.40~15.34%